# Effects of Protonation State on Electrocatalytic $CO_2$ Reduction by a Cobalt Aminopyridine Macrocyclic Complex

Jeffrey J. Liu‡, Alon Chapovetsky‡, Ralf Haiges‡, and Smaranda C. Marinescu*,‡

‡Department of Chemistry, University of Southern California, Los Angeles, California 90089, United States

*Corresponding Author: Smaranda C. Marinescu (smarines@usc.edu)

**KEYWORDS: $CO_2$ Reduction, Molecular Electrocatalysis, Proton Relays, Proton Transfer**

**ABSTRACT:** A critical component in the reduction of $CO_2$ to CO and $H_2O$ is the delivery of two equivalents of protons and electrons to the $CO_2$ molecule. The timing and sequencing of these proton and electrons transfer steps are essential factors in directing the activity and selectivity for catalytic $CO_2$ reduction. In previous studies we have reported a series of macrocyclic aminopyridine cobalt complexes capable of reducing $CO_2$ to CO with high faradaic efficiencies. Kinetic investigations reveal a relationship between the observed rate constant ($k_{obs}$) and the number of pendant amine hydrogen bond donors minus one, suggesting the presence of a deprotonated active catalytic state. Herein we investigate the feasibility of these proposed deprotonated states towards $CO_2$ reduction. Two deprotonated derivatives, **Co(L$^{4-}$)** and **Co(L$^{2-}$)**, of the tetraamino macrocycle **Co(L)** were independently synthesized and structurally characterized revealing extensive delocalization of the negative charge upon deprotonation. $^1$H NMR spectroscopy and UV-vis titrations studies confirm that under catalytic conditions, the active form of the catalyst gradually becomes deprotonated, supporting thus the $n_{donor} - 1$ relationship with $k_{obs}$. Electrochemical studies of **Co(L$^{4-}$)** reveal that this deprotonated analog is competent for electrocatalysis upon addition of an exogenous weak acid source, such as 2,2,2-trifluoroethanol, resulting in identical Faradaic efficiencies for $CO_2$-to-CO conversion to those observed with the fully protonated derivative (>98%).

## INTRODUCTION

Consumption of fossil fuels to meet the global energy demand is responsible for the release of approximately 37 Gt of $CO_2$ into the atmosphere annually resulting in unprecedented anthropogenic climate change.[1] The efficient capture and conversion of $CO_2$ to value added carbon containing products is widely recognized as a critical obstacle in moving towards sustainable fuel sources.[2] The process to convert $CO_2$ into usable materials and fuels requires breaking a relatively strong C=O double bond involving a high kinetic barrier.[3,4] Transition metal catalysts together with exogenous acid donors are often used to lower the energetic barriers to $CO_2$ reduction by coupling the C=O bond breaking step to either a C–H, C–C, or O–H bond forming step (such as in the formation of formate, oxalate, or $H_2O$). These broadly characterized proton coupled electron transfer reactions rely heavily on multiple proton and electron transfer steps, where timing and delivery of protons and electrons is dictated by the thermodynamic landscape and constitute critical factors in determining the catalytic rate and selectivity.[5]

To better understand and optimize how protons and electrons are delivered to $CO_2$ in transition metal catalysis, numerous studies utilize well defined homogeneous metal complexes as catalysts for $CO_2$ reduction in an effort to elucidate critical structure-function relationships, which may impact $CO_2$ reduction activity.[6–15] In nature, the metalloenzyme carbon monoxide dehydrogenase is known to catalyze the reversible two-electron two-proton reduction of $CO_2$ to CO and $H_2O$ at near zero overpotential.[16] A critical structural feature of the enzyme active site are a pair of hydrogen bonding amino acids residues (histidine and lysine) in the secondary coordination sphere, which interact with the coordinated $CO_2$ moiety (**Figure 1**).[17,18] Synthetic chemists have taken inspiration from these secondary coordination sphere elements in designing metal complexes for the activation of small molecules such as $O_2$, $N_2$, and $CO_2$[4,19–24] as well as to stabilize normally short lived reaction intermediates.[25–27] It has been well documented for synthetic $CO_2$ reduction catalysts that strategic positioning of proton relay groups in the secondary-coordination sphere positively influences, and enhances the rate of catalysis.[23,28–35] These proton relays are often proposed to directly interact with and stabilize the metal coordinated $CO_2$ analog,[7,23,31,33,36–38] or position exogenous acid molecules to interact with $CO_2$.[39–42] There are a large number of possible acid/proton relay pairs which may be used for $CO_2$ reduction, however, the largest enhancement in catalytic activity occurs when the orientation and p$K_a$ of the H-bond or proton relay group allows for rapid proton transfer.[33,43] Orientational or p$K_a$ mismatch of installed H-bond donor / proton relay groups may lead to negligible or even diminishing effects on catalytic rate.[31,33,44]

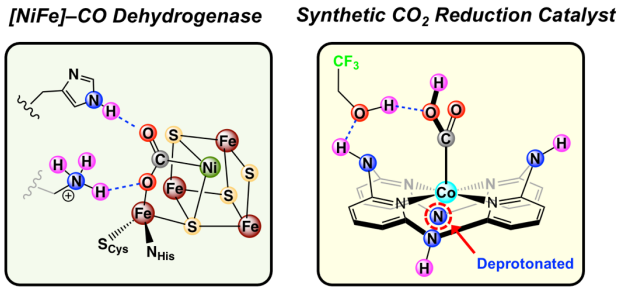


**Figure 1.** ChemDraw illustrations of the active site of [NiFe]–CO Dehydrogenase (left) and of a synthetic cobalt aminopyridine $CO_2$ reduction catalyst depicting the stabilizing influence of nearby hydrogen-bonding moieties for $CO_2$ binding (right).

In our previous studies we have examined the effect of tuning the number of pendant hydrogen bond donors with the rate of $CO_2$ reduction, as well as electronic inductive influences via covalent ligand modifications.[45–47] Using the macrocyclic aminopyridine cobalt complex **Co(L)** in DMF with 2,2,2-trifluoroethanol (TFE) added as an exogenous acid source (**Figure 2**), $CO_2$ was reduced to CO with high selectivity (98% Faradaic efficiency).[46] Computational studies reveal that the pendant amine protons serve to position a molecule of TFE to interact with the oxygen atoms of the cobalt coordinated $CO_2$ adduct, rather than directly hydrogen bond with $CO_2$ (**Figure 1**). This "pre-association" Co-($CO_2H^-$) adduct with TFE allows for eventual transfer of a proton from TFE to the coordinated hydroxycarbonyl intermediate ($CO_2H^-$) to cleave the C–O bond and eventually release CO and $H_2O$.

Kinetic studies where the number of pendant hydrogen bond donors was systematically varied through methylation of the secondary amines indicates the observed rate constant ($k_{obs}$) was linearly dependent on the number of available pendant amine hydrogen bond donors minus one, where the trimethylated derivative had the same activity as the tetramethylated complex. This relationship was attributed to the acidity of the pendant amine protons, which were hypothesized to undergo deprotonation upon dissolution, indicating that both the trimethylated and tetramethylated complex have no available proton relays to hydrogen bond with TFE.

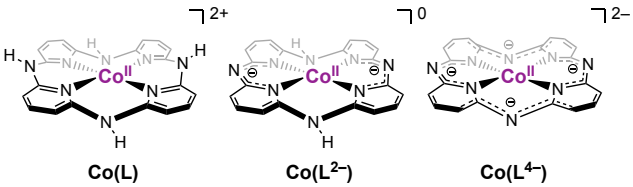


**Figure 2.** ChemDraw illustrations of the complexes discussed in this work.

The existence of a deprotonated state is suggested by kinetic experiments, however, no direct isolation of a deprotonated intermediate was reported. Solid state characterization indicates no evidence of macrocyclic deprotonation, and solution p$K_a$ measurements, while suggestive of a low initial p$K_a$, where not performed under catalytic conditions in the presence of TFE.[45,46]

Herein we structurally isolate and characterize the deprotonated analogs of **Co(L)** and examine the effects of protonation state both on the chemical structure and the electrochemical activity. Investigation into the solution state protonation under catalytic conditions reveal the mechanistic origin of the $n_{donor} - 1$ relationship with the observed rate constant. These deprotonated complexes are shown to exhibit a catalytic current response under $CO_2$ and in the presence of TFE, indicating they are competent $CO_2$-reduction catalysts.

## RESULTS AND DISCUSSION

### Synthesis and Structural Characterization of Co(L$^{2-}$) and Co(L$^{4-}$)

Synthesis of the doubly deprotonated complex **Co(L$^{2-}$)** was accomplished through addition of excess NaH (60% wt. in paraffin) to a solution containing the tetra NH complex **Co(L)** in pyridine under an $N_2$ atmosphere. The mixture was sonicated and monitored by $^1$H NMR spectroscopy in pyridine-$d_5$ until all features corresponding to the starting **Co(L)** complex had disappeared (δ 42.21, 5.40, and – 15.16 ppm) and replaced by a sharp peak at δ 4.44 ppm, assigned to dissolved $H_2$, and a broad paramagnetic resonance at δ 10.90 ppm, attributed to **Co(L$^{2-}$)** (**Figure S1**).

Filtration of the reaction mixture and diffusion of diethyl ether into the resulting filtrate led to the emergence of dark red needles (**Scheme 1**), which exhibited $^1$H NMR resonances at δ 9.56 and –1.23 ppm in DMSO-$d_6$. An Evans method experiment reveals the effective magnetic moment ($\mu_{eff}$) had changed from 4.99 $\mu_B$ for **Co(L)** to 2.13 $\mu_B$ for **Co(L$^{2-}$)**, reflecting a spin state change for the d$^7$ metal complex from high-spin S = 3/2 to low spin S = 1/2.

A solid-state structure was obtained via X-ray diffraction revealing an overall Jahn-Teller distorted six-coordinate complex where the meridional positions are occupied by the macrocyclic aminopyridine ligand, and the axial positions are filled by two weakly coordinating pyridine moieties (**Figures 3A** and **S18**). A strong Jahn-Teller effect is expected for six-coordinate low-spin d$^7$ ions arising from the single $e_g$ electron, and indeed both axial pyridines are elongated with Co–N distances greater than 2.2 Å.[48] No counterion was observed in the X-ray structure, supporting a cobalt(II) oxidation state and an overall neutral complex, with two deprotonated moieties (**Figure 3A**). Solid state packing also hints at the evidence of intermolecular hydrogen bonding interactions between adjacent macrocyclic molecules. The donor acceptor distance between adjacent protonated and deprotonated pendant amines is approximately 2.829 Å with an N–H–N angle of 165.3(1)º (**Figure S18**) which are in the range for a hydrogen bond,[49] and further corroborates the doubly deprotonated state of **Co(L$^{2-}$)**.

**Scheme 1. Synthetic scheme for the generation of Co(L$^{4-}$) and Co(L$^{2-}$) from Co(L).**

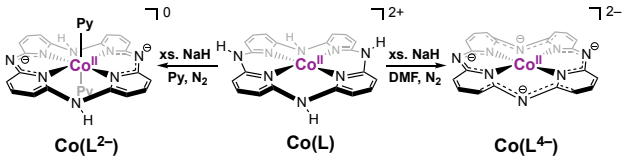


Two distinct bonding environments within the **Co(L$^{2-}$)** macrocyclic scaffold arise. The deprotonated pedant N-atom bridge distorts to have one slightly longer (1.363(5) Å) and one slightly shorter (1.342(5) Å) $C_{py}$–$N_{bridge}$ bond, while the protonated site (NH) contains two long $C_{py}$–$N_{bridge}$ bonds (1.383(5) and 1.378(5) Å) (**Table 1** and **Figure S20**). This observation is consistent with the emergence of an imine-like

structure upon deprotonation of the pendant amine, where the electrons from the former N–H bond are not completely localized on the nitrogen atom, and are donating into the macrocyclic pyridyl π-system.

Synthesis of the fully deprotonated complex **Co(L$^{4-}$)** was achieved through the addition of excess NaH (60% wt. in paraffin) to a solution of **Co(L)** in DMF under an $N_2$ atmosphere. The solution was allowed to stir for 72 hours and was subsequently filtered and crystalized via vapor diffusion of diethyl ether into the reaction mixture, yielding dark brown-purple needles. The ability to isolate the fully deprotonated complex, **Co(L$^{4-}$)**, under these conditions is attributed in part to the longer reaction time (72 *vs* 1 hour) with NaH and use of DMF rather than pyridine as solvent. Structural characterization of **Co(L$^{4-}$)** was accomplished via X-ray diffraction revealing a distorted 4-coordinate square-planar complex (**Figure 3B**). Each bridging amine is deprotonated and coordinated to a sodium atom (2.436(2) Å), which in-turn bridges to an adjacent cobalt macrocycle in the solid state (**Figure S19**). The average Co–$N_{py}$ bond length in **Co(L$^{4-}$)** is 1.939(2) Å, reflecting a slight decrease relative to the one observed in **Co(L)** (1.951(4) Å). The bridging C–N bonds also change due to the nitrogen deprotonation resulting in one slightly shorter (1.335(3) Å) and one slightly longer (up to 1.384(3) Å) $C_{py}$–$N_{bridge}$ bond (**Table 1**), suggesting delocalization of the negative charge into the pyridyl moieties. This is further supported by the appearance of a puckering in the pyridyl fragment where up to a –17.2º in-plane torsion angle is observed *vs.* a –6.8º angle found in the tetra NH complex **Co(L)** (**Table 1**). Tracking the tau parameter (τ = 0 for square pyramidal and square planar complexes, and τ = 1 for trigonal bipyramidal and tetrahedral complexes),[50,51] reveals successive deprotonation results in a deviation from square planarity. These structural parameters indicate that following deprotonation the negative charge is no longer solely localized at the bridging nitrogen atoms and are rather delocalized across the ligand structure.

**Table 1. Selected structural parameters for Co(L), Co(L$^{2-}$) and Co(L$^{4-}$) derived from Figure 3. See Figure S20 for additional details. [a]$N_{py}$ refers to pyridyl nitrogen atoms N1, N1′, N3 or N3′. [b]$C_{py}$ refers to C1, C1′, C5, C5′, C6, C6′, C10 or C10′. [c]$N_{bridge}$ refers to N2, N2′, N4, and N4′. [d]Deprotonated $N_{bridge}$ atom, N4. [e]Calculated excluding weakly coordinating axial pyridine moieties.**

| | $d_{avg}$(Co-$N_{py}$)[a] (Å) | d($C_{py}$-$N_{bridge}$)[b,c] (Å) | d($C_{py}$-$N_{py}$) (Å) | Pyridyl Torsion (º) | τ[50,51] |
|---|---|---|---|---|---|
| **Co(L)** | 1.951(4) | 1.399(3) | 1.342(3) | −6.8 | 0 |
| **Co(L$^{2-}$)** | 1.959(3) | 1.383(5)<br>1.378(5)<br>1.363(5)[d]<br>1.342(5)[d] | 1.366(5)<br>1.362(5)<br>1.360(5)<br>1.360(4) | 9.3 | 0.04[e] |
| **Co(L$^{4-}$)** | 1.939(2) | 1.384(3)<br>1.376(3)<br>1.336(3)<br>1.335(3) | 1.392(3)<br>1.388(3)<br>1.378(3)<br>1.376(3) | −17.2 | 0.18 |

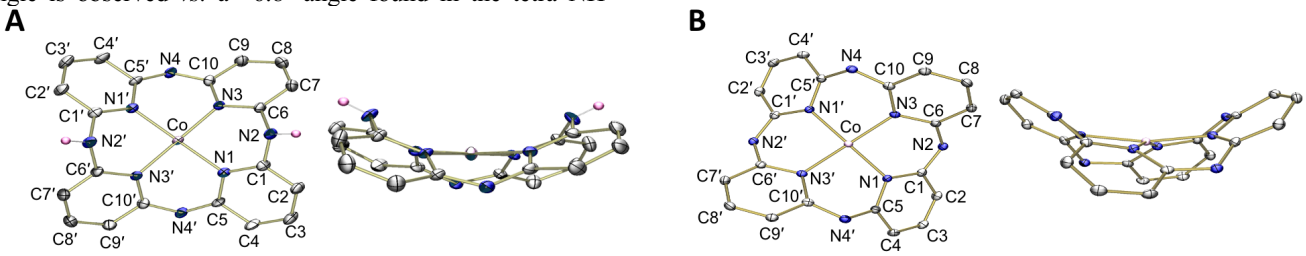


**Figure 3.** Side-on and top-down thermal ellipsoid diagram for **Co(L$^{2-}$)** displayed at the 50% probability level. A figure showing both axial pyridines and intramolecular hydrogen-bonding is shown in **Figure S18**. Non-labile hydrogen atoms and axial pyridines are omitted for clarity (**A**). Side-on and top-down thermal ellipsoid diagram for **Co(L$^{4-}$)** displayed at the 50% probability level. Non-labile hydrogen atoms, and DMF solvated sodium cations are omitted for clarity (**B**). Selected bond lengths and torsion angles can be found in **Table 1** and **Figure S20**.

### $^1$H NMR Characterization of Co(L$^{4-}$)

The solution phase structure of **Co(L$^{4-}$)** was explored via $^1$H NMR spectroscopy. The $^1$H NMR spectrum of **Co(L)** in DMSO-$d_6$ reveals two sharp resonances at δ 30.93 and –1.35 ppm (**Figure S2**), which after treatment with NaH in DMF and recrystallization with diethyl ether, reveals two features at δ 9.74 and –1.81 ppm, attributed to **Co(L$^{4-}$)**. Evans method experiments measuring solution phase magnetic moment reveal that **Co(L$^{4-}$)** possesses a $\mu_{eff}$ of 2.67 $\mu_B$, which lies in between the expected range for a low-spin (S = 1/2) and high spin (S = 3/2) complex.[52] We postulate there may be an equilibrium between the high-spin and low-spin complexes, however variable temperature NMR experiments indicate virtually no change in the magnetic moment over an 80 ºC window from –60 ºC to 20 ºC (**Figure S3, Table S1**). This result may indicate that either the spin-crossover temperature is outside of the experimentally studied temperature range, or that more complicated intermolecular interactions may be occurring to give the unusual (for $d^7$ cobalt) observed magnetic moment.

To characterize the effects of protonation state on solution phase structure, titrations with a strong acid, HOTf•DMF ($HDMF^+$), were carried out in DMSO-$d_6$. Upon addition of one equivalent $HDMF^+$, a decrease in intensity and broadening of the $^1$H features of **Co(L$^{4-}$)** occurs (**Figure 4**). Addition of two equivalents of $HDMF^+$ results in broadening and eventual disappearance of the original peaks attributed to **Co(L$^{4-}$)**. Attempts to generate these intermediate spectra from independently isolated **Co(L$^{2-}$)** with exogenously added $NaBF_4$ were unsuccessful (**Figure S26**) suggesting the resulting species is not equivalent to the independently generated complex. The exact causes for this difference are unclear, but we would like to note that addition of two equivalents of strong acid does not necessarily generate a doubly protonated species; it is possible addition of $HDMF^+$ generates mixtures of singly, doubly, triple, and fully protonated complexes which all exist in dynamic equilibrium. Subsequent addition of pyridine-$d_5$ (20 equiv.) to a mixture of

**Co(L$^{4-}$)** with two equivalents of HDMF$^+$ does not lead to any significant further changes, as observed by $^1$H NMR spectroscopy (**Figure S27**).

Further addition of a third equivalent of HDMF$^+$ leads to weak and broad features that are paramagnetically shifted at approximately δ 30 and 25 ppm, while four equivalents of acid lead to sharp features at δ 30.93 and –1.35 ppm, which closely matches that of the authentic tetra NH complex **Co(L)** (**Figure 4**). The recovery of **Co(L)** from **Co(L$^{4-}$)** following the addition of four equivalents HDMF$^+$ affirms the assignment of **Co(L$^{4-}$)** existing in a quadruple deprotonated state in solution.

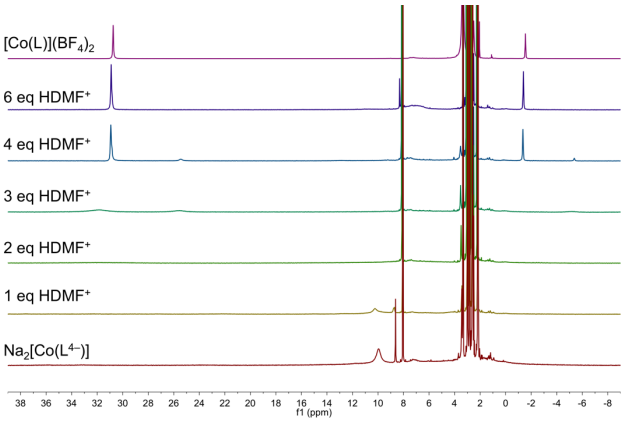


**Figure 4.** $^1$H NMR spectrum of **Co(L$^{4-}$)** (titrated with HOTf•DMF in DMSO-$d_6$ under $N_2$. Following the first equivalent of acid the features corresponding to **Co(L$^{4-}$)** broaden, and completely disappear by the addition of the second equivalent. Addition of a third equivalent of acid results in the emergence of weak and broad paramagnetically features, while addition of the fourth equivalent yields shifts consistent with authentic **Co(L)**.

### Solution FTIR Spectroscopy of Co(L$^{4-}$)

The solution phase structure of **Co(L$^{4-}$)** was further verified through solution FTIR spectroscopy. An air-free solution of **Co(L$^{4-}$)** in acetonitrile was prepared and an FTIR spectrum was collected and compared to that of **Co(L)** in an acetonitrile solution (**Figure 5**). The as prepared spectrum of **Co(L)** shows a characteristic broad peak at 3334 cm$^{-1}$, which is assigned to a $\nu_{NH}$ stretching vibration. This feature is absent in the spectrum of independently synthesized **Co(L$^{4-}$)**, consistent with the deprotonation of the pendant amine. The split feature near 3600 cm$^{-1}$ in **Co(L)** is attributed to adventitious $H_2O$, which is expected, as the **Co(L)** solution (unlike the **Co(L$^{4-}$)** solution) was prepared under ambient conditions.

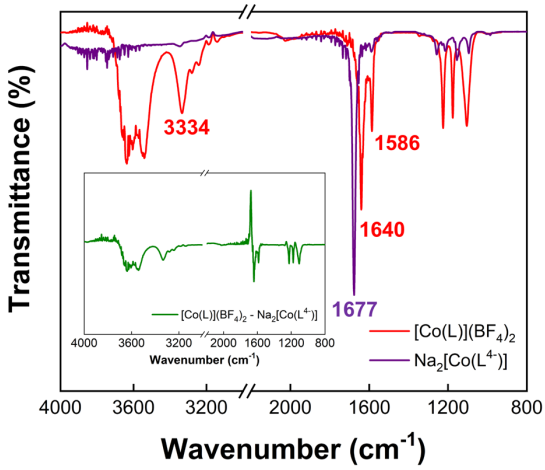


**Figure 5.** Solution FTIR spectra of **Co(L)** (red) and **Co(L$^{4-}$)** (purple) in acetonitrile. Inset: The difference spectrum (green) between **Co(L)** and **Co(L$^{4-}$)**.

The two peaks at 1640 cm$^{-1}$ and 1586 cm$^{-1}$ in the **Co(L)** spectrum are assigned to the pyridyl ring vibrations, which disappear upon deprotonation of **Co(L)** to **Co(L$^{4-}$)**, and a sharp peak at 1677 cm$^{-1}$ emerges. These observations are consistent with the solid-state crystal structure data, where upon full deprotonation of **Co(L)** there is delocalization of negative charge into the pyridine ring, and an increase in the bond order between the bridging pendant nitrogen and the pyridyl carbon atom as indicated by a shortening of the C–N bond.

### Spectrophotometric Titration of Co(L$^{4-}$) with HOTf•DMF

UV-vis spectroscopy was employed to study the electronic structure of **Co(L$^{4-}$)** and its protonated intermediates. When **Co(L$^{4-}$)** is dissolved in DMF, an orange amber solution arises which contains two prominent absorption features at 310 nm (30,800 M$^{-1}$ cm$^{-1}$) and 404 nm (32,700 M$^{-1}$ cm$^{-1}$) (**Figure S4**). Upon addition of 0.9 to 1.9 equivalents of HDMF$^+$, a slight decrease of the peak at 404 nm occurs, coupled with the appearance of a sharp peak at 376 nm (**Figure 6**). Addition of 2.8 equivalents of acid results in the disappearance of the peak at 310 nm, and a significant decrease of the 404 nm absorbance, coupled with the emergence of a new peak centered at 334 nm. Approximately four equivalents of HDMF$^+$ results in further increase of the 334 nm feature, coupled with complete loss of the 310 nm band, and conversion of the 404 nm absorbance to a weak shoulder. Addition of slight stoichiometric excess (5.6 equiv.), and large excess (940 equiv.) of HDMF$^+$ results in the complete loss of the shoulder feature at 404 nm, and minimal increase of the 334 nm peak, indicating roughly four equivalents of acid are required to fully protonate the complex. This conclusion is supported by comparing the UV-vis spectra of **Co(L$^{4-}$)**, where greater than ~4 equivalents of HDMF$^+$ is titrated, to a solution of authentic **Co(L)** (**Figure 6 inset**).

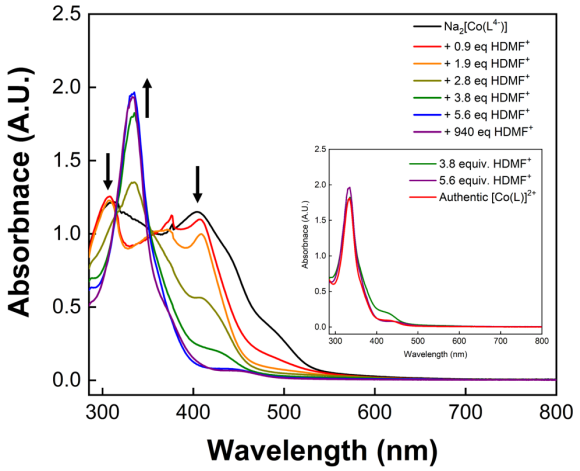


**Figure 6.** UV-vis spectroscopy of **Co(L$^{4-}$)** (35 μM) titrated with HOTf•DMF in DMF under $N_2$. Inset: Comparison of authentic **Co(L)** with **Co(L$^{4-}$)** + 3.8 equiv. HOTf•DMF, and 5.6 equiv HOTf•DMF showing approximately four equivalents of acid are required to convert to the tetra NH species.

**Spectrophotometric Calculation of p$K_a^1$ for Co(L)**

Titration studies of **Co(L$^{4-}$)** with the strong acid HOTf•DMF ($HDMF^+$) indicate that four equivalents of acid are required to convert **Co(L$^{4-}$)** to **Co(L)**. However, many catalytic conditions for electrocatalytic $CO_2$ reduction utilize weaker acids as to avoid concomitant hydrogen evolution. To study the effects of these weaker acids on protonation state, spectrophotometric titrations of **Co(L$^{4-}$)** with 2,2,2-trifluoroethanol (TFE) were performed (**Figure 7**).

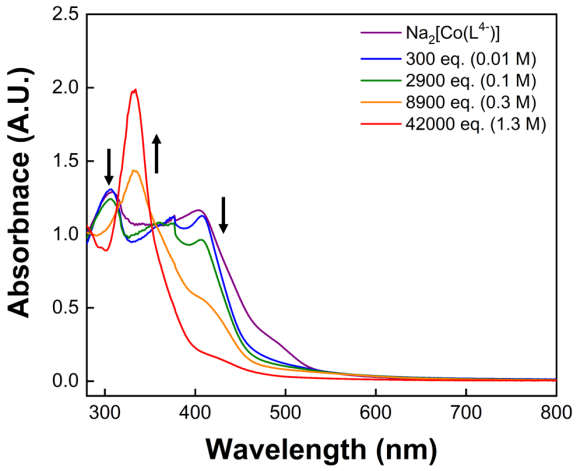


**Figure 7.** UV-vis spectroscopy of **Co(L$^{4-}$)** (35 μM) titrated with large excess of 2,2,2-trifluoroethanol (TFE). To fully convert **Co(L$^{4-}$)** to **Co(L)** large excess of TFE (42,000 equivalents, 1.3 M) is required.

Unlike the titrations with HOTf•DMF where a stoichiometric amount of acid was needed per equivalent of deprotonated pendant amine, UV-vis titrations indicate that a large excess of TFE (42,000 equivalents, 1.3 M) is necessary to convert **Co(L$^{4-}$)** to the tetra NH complex **Co(L)**. This non-stoichiometric conversion of **Co(L$^{4-}$)** to **Co(L)** coupled with the characteristic absorbance of **Co(L)** at 334 nm allows for the extrapolation of a p$K_a$, where sufficient TFE is added to yield an approximate binary system of **Co(L)** with its mono-deprotonated conjugate base, **Co(L$^-$)**. Spectroscopically these conditions occur when 0.3 M TFE (8900 equiv.) is added as indicated by the incomplete emergence of the characteristic 334 nm band of **Co(L)**, suggesting **Co(L)** and **Co(L$^-$)** are in equilibrium with TFE and $TFE^-$ (the conjugate base of TFE). By using the absorbance at 334 nm as a spectroscopic handle, the speciation of **Co(L)**, **Co(L$^-$)**, TFE and $TFE^-$ can be determined and a p$K_a^1$ value of 20.55 ± 0.06 in DMF is extrapolated (**Figures S5A, S22, Scheme S1, and Table S2**). This value indicates the pendant proton relay is intrinsically much more acidic than the added acid source TFE (p$K_a$ = 23.45 in DMSO)[53] and will likely remain deprotonated after any proton consuming process, unless a very large excess of TFE is added. The same extrapolation was performed in DMSO (**Figures S5B, S21, S22, Table S3**) and yielded a p$K_a^1$ value of 20.50 ± 0.06. This value differs from our previously reported[46] one for **Co(L)** (2.74), which was measured under aqueous conditions. We believe these new p$K_a^1$ values in organic solvents (DMF and DMSO) more accurately reflects the relevant protonation behavior of **Co(L)** under the non-aqueous catalytic conditions. It is important to note that the tabulated p$K_a^1$ value is benchmarked to the reported p$K_a$ of TFE in DMSO, which assumes infinite dilution. The true p$K_a^1$ under catalytically relevant conditions (1 atm $CO_2$, > 1 M TFE) is likely higher due to homoconjugation of TFE and interactions with $CO_2$ (*vide infra*).[54]

**Cyclic Voltammetry Characterization of Co(L$^{4-}$)**

To better understand the electrochemical properties of these isolated deprotonated complexes, cyclic voltammetry (CV) was utilized to quantify the effects of protonation state on redox behavior. In a typical experiment 0.5 mM of the metal complex was dissolved in a solution of DMF containing 0.1 M [$n$Bu$_4$N][$PF_6$] with ferrocene (Fc) as an internal standard, and all potentials were measured versus the $Fc^{+/0}$ couple. All CVs were performed using a three-electrode system containing a glassy carbon working electrode, platinum wire counter electrode, and silver wire pseudo reference electrode.

Cyclic voltammograms of **Co(L$^{4-}$)** reveal a significant shift in the $Co^{II/I}$ reduction from the reversible couple at –1.66 V in the tetra NH complex to an irreversible and ill-defined wave with multiple weak and broad reductive features past (more negative than) –2.1 V (**Figure S6**). Log-log plot analysis of this reduction feature is consistent with a freely diffusing species (**Figure S7**). The poor resolution of this feature suggests **Co(L$^{4-}$)** may exhibit extensive intermolecular interactions in the solution phase, resulting in a broadening of potentials at which reduction occurs. Scanning to further negative potentials reveals no apparent feature for the $Co^{I/0}$ reduction event within the solvent window and a cross-over point appears upon the return scan (**Figure S6**). Curve crossing in cyclic voltammetry is indicative of complex downstream reaction chemistry where the identity of the chemical species changes such that an electrochemical step no longer restores the original species on the return scan.[55] The return oxidative scan reveals multiple oxidative features at –1.04, –0.70, and –0.41 V. Log-log plot analysis from variable scan rate experiments (VSR) indicate these features are molecular in nature, and correspond to freely diffusing species in solution (**Figure S8**). Direct assignment of these oxidation features is difficult as they occur following the crossover point, which indicates a complex change in the nature solution species within the diffusion layer. Subsequent scanning cycles reveal new redox couples, which increase in intensity over successive scans (**Figure S9**). Log-log plot analysis of

current vs scan rate yield slopes of near unity, consistent with a surface immobilized species pointing to the deposition of an electroactive material (**Figure S9**). Re-polishing of the electrode after deposition leads to satisfactory replication of the original voltammogram containing curve crossing (**Figure S10**), although with slightly lower intensity.

Titration of HOTf•DMF to a solution of **Co(L$^{4-}$)** restores the reversibility of the $Co^{II/I}$ potential and gradually shifts it to more positive potentials, eventually settling at –1.66 V *vs.* $Fc/Fc^{+}$, the reported $Co^{II/I}$ potential for **Co(L)**, when > 4 equiv. of HOTf•DMF are titrated (**Figure 8**). The titrated equivalents of HDMF•DMF can be viewed as a surrogate for the bulk protonation state of **Co(L$^{4-}$)**, where increasing the electric charge of the molecule allows more favorable reduction.

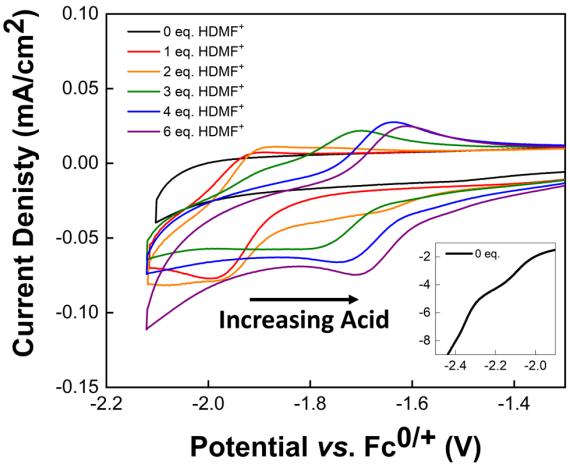


**Figure 8.** Cyclic voltammogram of **Co(L$^{4-}$)** (0.5 mM) titrated with HOTf•DMF ($HDMF^{+}$) under a $N_2$ atmosphere with 0.1 M $n$Bu$_4$NPF$_6$ in DMF. Inset the reduction feature ascribed to the $Co^{II/I}$ reduction in the absence of added acid.

**Catalytic Cyclic Voltammetry Studies of Co(L$^{4-}$) with TFE and $CO_2$**

To test the viability of the deprotonated states of **Co(L)** as an electrocatalysts for $CO_2$ reduction, titrations with TFE under $CO_2$ were performed and examined via cyclic voltammetry. When TFE was titrated into a solution of **Co(L$^{4-}$)**, a significant current increase was observed at –2.66 V *vs.* $Fc^{0/+}$, analogous to the catalytic behavior observed in studies of **Co(L)** complex (**Figure 9A**). Regeneration of **Co(L)** via addition of four equiv. HOTf•DMF followed by TFE titration yielded a nearly identical response with a current density of 18-19 mA/cm$^2$ when 1.5 M TFE is added (**Figure 9B).** A normalized current (**Figure 9C**) can be calculated from the voltammogram in **Figure 9B** corresponding to a maximum $i_{cat}/i_p$ value of 188.3, which is similar to the reported value for the mono-alkylated macrocycle derivative (189.9) and just below the value for authentic **Co(L)** (208.8).[46] This small discrepancy (lower normalized current for the *in situ* generated **Co(L)**) may be linked either to incomplete protonation of the initial **Co(L$^{4-}$)** from $HDMF^{+}$, or partial catalyst deposition from the initial CV scans taken prior to acid addition. An $i_{cat}/i_p$ plot could not be generated from **Figure 9A** due to the absence of a reversible cobalt couple under $N_2$ atmosphere.

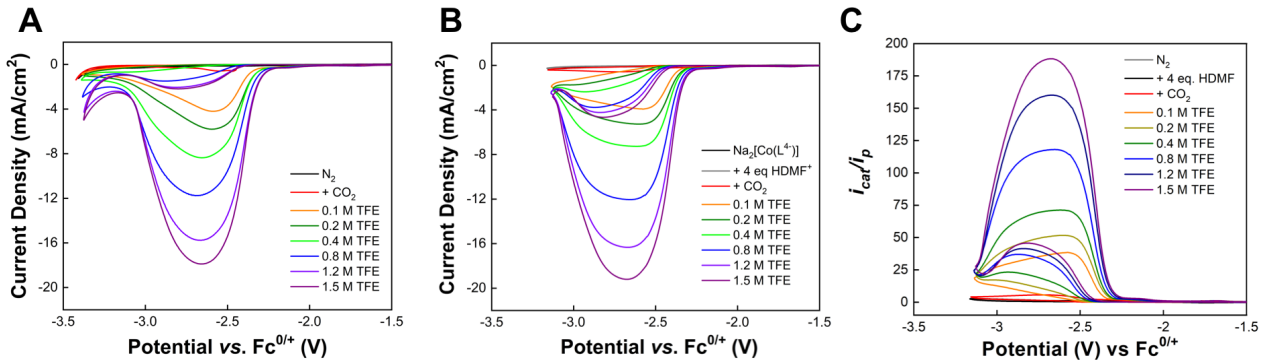


**Figure 9.** Cyclic voltammograms of **Co(L$^{4-}$)** (0.5 mM) in a DMF solution containing 0.1 M [$n$Bu$_4$N][PF$_6$] titrated with TFE (0 – 1.5 M) under 1 atm $CO_2$ (A). Addition of 4 equivalents of HOTf•DMF to **Co(L$^{4-}$)** in a DMF solution containing 0.1 M [$n$Bu$_4$N][PF$_6$] to generate **Co(L)** *in situ*, followed by titration with TFE (0 – 1.5 M) under 1 atm $CO_2$ (B). The normalized current, $i_{cat}/i_p$ for the reaction for **Co(L$^{4-}$)** + 4 equivalents of HOTf•DMF (C).

**Controlled Potential Electrolysis of Co(L$^{4-}$) for Catalytic $CO_2$ to CO Conversion**

While similar catalytic current responses were observed between **Co(L$^{4-}$)** and the *in situ* generated **Co(L)** titrating with TFE and under a $CO_2$ atmosphere, it is unknown what effects deprotonation of the bridging amines would have on catalytic selectivity, and in particular the Faradaic efficiencies during catalysis. Thus, controlled potential electrolysis (CPE) experiments were conducted to answer this question.

**Table 2. Faradaic efficiencies for controlled potential electrolysis experiments with Co(L) and Co(L$^{4-}$). Experiments were conducted under 1 atm $CO_2$, 1.5 M TFE, 0.5 mM [Co] with 0.1 M $n$Bu$_4$NPF$_6$ in DMF. Electrolysis was conducted at –2.75 V *vs.* Fc/Fc$^{+}$ for 60 min. [a] Values from reference 46.**

| | Charge (C) | μmol CO | $FE_{CO}$ (%) | μmol $H_2$ | $FE_{H2}$ (%) |
|---|---|---|---|---|---|
| **Co(L)**[a] | 30.9 | 157 | 98.0 | 0 | 0.0 |
| **Co(L$^{4-}$)** | 56.2 | 287 | 99.7 | 8.9 | 3.0 |

Controlled potential electrolysis at –2.75 V *vs.* $Fc^{+/0}$ ($\eta_{CO2/CO}$ = 2.02 V)[56] of a solution of **Co(L$^{4-}$)** under a $CO_2$ atmosphere and 1.5 M TFE reveal high Faradaic efficiency for $CO_2$ to CO conversion (99.7%) over the course of 60 min with a small amount (~3 %) of $H_2$ formation **(Figures S11** and **S12)**. These Faradaic efficiencies and overall catalytic selec-

tivity are analogous to the previously reported cobalt aminopyridine macrocycles containing at least one pendant amino group.[46] The larger amount of charge passed, and moles of CO produced for **Co(L$^{4-}$)** compared to **Co(L)** is attributed to differences in the area of the working electrode exposed to solution which stems from large differences in the working cell geometry between the two experiments. As such, only the Faradaic efficiencies may be directly compared, as the measured current is not normalized by the effective surface area.

A closer examination of the CPE current *vs*. time plot reveals the current decreases approximately 45% over the course of one hour (**Figure S11**). Qualitative scanning electron microscopy (SEM) and energy-dispersive X-ray spectroscopy (EDS) of the rinsed electrode surface suggests the presence of amorphous cobalt on the washed electrode surface (see the supporting information for further discussion of the SEM/EDS results). While we cannot quantify the amount of cobalt on the surface, post-electrolysis cyclic voltammograms and UV-vis spectra of the working solution indicate the majority of the cobalt catalyst remains homogeneous in nature.

Analysis of the pre-electrolysis working compartment solution reveal that the addition of TFE (1.5 M) to **Co(L$^{4-}$)** results in an absorption spectrum, termed as the pre-CPE solution, which closely resembles that of the doubly deprotonated state (**Figures 6** and **10A**). Taking into account the concentration of cobalt catalyst (0.5 mM) and the volume of the working compartment solution (25 mL), the observed UV-vis spectra is consistent with titration experiments (**Figure 7**) where approximately 3000 equivalents of TFE are added. Note the concentration of the cobalt catalyst in the UV-vis experiment (35 μM) is significantly lower than that for an electrolysis experiment (0.5 mM) resulting in a lower concentration of TFE (0.1 M) required for ~3000 equivalents with respect to cobalt in the UV-vis experiment.

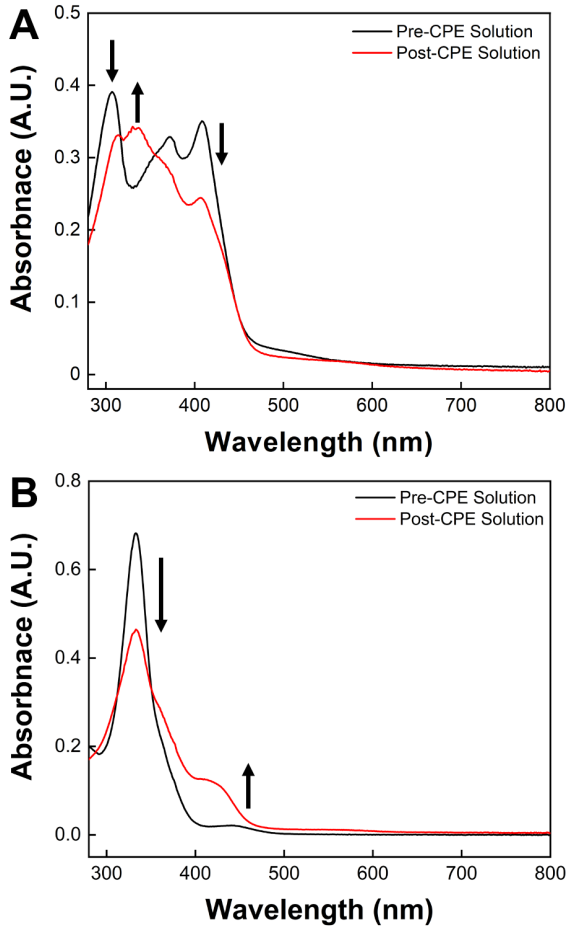


**Figure 10.** UV-vis spectra of the pre- and post-CPE working compartment solution of **Co(L$^{4-}$)** (**A**) or **Co(L)** (**B**) containing 1.5 M TFE in a 0.1 M $n$Bu$_4$NPF$_6$ DMF solution under a $N_2$ atmosphere, followed by introduction of $CO_2$, and 60 minutes of electrolysis at –2.75 V *vs*. $Fc^{+/0}$. The presence of TFE (3000 equiv.) rapidly protonates **Co(L$^{4-}$)**, yielding a spectrum consistent with the doubly deprotonated analogue.

Following 60 minutes of CPE at –2.75 V *vs.* $Fc^{+/0}$ the absorption spectrum of the working solution, termed as post-CPE solution, was reexamined and reveals a partial decay of the double deprotonated species with features at 307 and 408 nm, and the growing in of a broad peak at ~334 nm. This new peak combined with the appearance of a shoulder in the absorption at 408 nm have similarities to the singly deprotonated species, suggesting a mixture of the doubly and singly deprotonated species are in solution post-catalysis (**Figure 10A**). While surprising, this increase in bulk catalyst protonation state can be attributed to homoconjugation by TFE in the presence of $CO_2$.[54] Goddard and co-workers have calculated that in acetonitrile, the acidity of TFE when > 1 M TFE is present can increase by more than 10 p$K_a$ units in the presence of $CO_2$.[54] Such effects stem from the stabilization of the conjugate base (2,2,2-trifluoroethanoate in the case of TFE) with $CO_2$ to give an organocarbonate product, akin to carbonic acid formed from equilibrium solutions of dissolved $CO_2$ in $H_2O$. Indeed, addition of $CO_2$ to a solution containing **Co(L$^{4-}$)**, 1.2 M TFE, and 0.1 M [$n$Bu$_4$N][PF$_6$] under $N_2$ fully re-protonates the complex yielding **Co(L)** (**Figure S23**). Addition of 25 equivalents of $H_2O$, the byproduct formed from $CO_2$-to-CO conversion, does not appear to affect the speciation. Thus, while it appears the bulk protonation state

had increased during catalysis (**Figure 9A**), the addition of $CO_2$ likely protonates the majority of complex to **Co(L)**, which then becomes deprotonated over the course of electrolysis. This observation also explains why similar current densities are measured from the CV titration experiments of **Co(L$^{4-}$)** and the *in situ* generated **Co(L)** from the addition of four equivalents of $HDMF^+$, despite the former initially existing in a lower protonation state.

Analogous tandem CPE/UV-vis experiments with **Co(L)** reveals a decrease in the absorption at 334 nm and the growing in of a shoulder feature near 410 nm, yielding a post-CPE spectrum with features resembling a mixture of the fully protonated complex and singly deprotonated complex (**Figure 10B**). This can be rationalized by deprotonation of a pendant amine group either directly by a putative cobalt coordinated hydroxycaronbyl adduct, or by the *in-situ* generated 2,2,2-trifluoroethanoate. Separate experiments of **Co(L)** with sodium triflouroethanote reveal it is capable of deprotonating **Co(L) (Figure S13)**. The differences in final electrolysis speciation (**Figures 10A** and **10B**) are likely due to the sensitivity of the TFE re-protonated complex to the concentration of TFE and $CO_2$. As both $CO_2$ and TFE are consumed during electrolysis, the bulk solution catalyst protonation state for the TFE re-protonated complex is expected to decrease faster than authentic **Co(L)**.

**Mechanistic Significance of a Deprotonated Complex**

Our previous studies have found a linear relationship between $k_{obs}$ and the $n_{donor} - 1$, implying the active form of the catalyst has one fewer available pendant hydrogen bond donor, and that the active form of the catalyst is singly deprotonated. Our results here indicate **Co(L)** exists as the tetra NH complex in solution, as evidenced by UV and $^1$H NMR spectroscopy studies, as well as by $HDMF^+$ titrations with **Co(L$^{4-}$)**. It is likely that upon the first cycle of electrocatalysis, one of the pendant protons is consumed and the resulting singly deprotonated species is unable to be re-protonated by TFE, which is a weaker acid by nearly three orders of magnitude (**Figure 11**). Homoconjugative effects may increase the acidity of TFE, however, the increase in acidity is not able to compensate for the TFE, and $CO_2$ consumption over the course of the reaction. This is evidenced by the post-electrolysis UV-vis spectrum of the working cell solution revealing that the cobalt complex exists as a mixture of the singly and doubly deprotonated states.

To confirm simple electrolysis results in the deprotonation of the ligand, CPE under non catalytic conditions ($N_2$, no acid) was performed (**Figures S14-15**). Post electrolysis UV-vis analysis reveals the resultant solution had features consistent with a mixture containing the singly deprotonated species (**Figure S17**), while a negative shift in the $Co^{II/I}$ couple (**Figure S15**), and detection of a small amount of $H_2$ (**Figure S16**), are consistent with a reductive deprotonation process upon reduction to a $Co^0$ species. This may be an explanation as to why the $Co^{I/0}$ couple is irreversible[45] – upon reduction to $Co^0$ a fast deprotonation chemical reaction takes place producing $H_2$, whereby on the return scan the original $Co^0$ no longer exists.

The timing and delivery of protons and electrons to the metal center is a crucial factor in determining catalytic rate and selectivity. Recently, Queyriaux, Artero and coworkers have demonstrated for a similar, although non-cyclic, cobalt aminopyridine complex that the pathway for hydrogen evolution is greatly dependent on the acidity of the exogenous acid.[57] Reduction of $CO_2$ under acidic conditions must balance the concentration of acid required to protonate the metal-bound $CO_2$ adduct, with the propensity of the reduced metal center reacting with protons to make $H_2$. While stronger acids may more readily react with reduced metal coordinated $CO_2$ adducts to make CO and $H_2O$, they may also yield metal hydride intermediates, which can continue to react to give $H_2$ or formate, lowering the catalytic selectivity.

Hydrogen bonding either directly through intramolecular pendant proton relays or indirectly through intermolecular hydrogen bonding networks elegantly sidestep the requirement for a strong acid by positioning a weaker acid to spatially interact with the coordinated substrate (*e.g.* $CO_2$). By using weaker acid sources for catalysis, it is less likely for the added acid to promote hydrogen evolution via direct protonation. The role of acid homoconjugation and reactivity with $CO_2$ is also an important factor as the increased acidity in the presence of $CO_2$ allows for utilizing weaker acids that do not directly promote hydrogen evolution.

The use of weaker acids is not without limitation, as they may allow for deprotonation of pendant relays resulting in catalyst deprotonation. As described above, the deprotonated forms of **Co(L)** are less electrochemical stable and are prone to deposition (**Figures S9, S11, S25-S26**). Further studies are required to balance the strength of the exogenous acid donor to preclude deprotonation, while maintaining product selectivity.

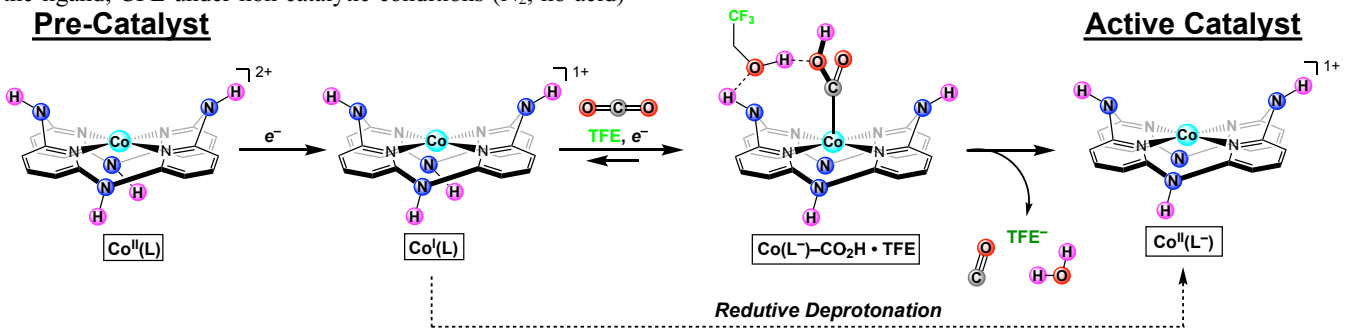


**Figure 11.** Proposed mechanistic pathway for the pre-catalytic deprotonation of **Co(L)** to generate the singly deprotonated **Co(L$^-$)** active catalytic state. The two-electron reduction of **Co(L)** generates an active $Co^0$ intermediate, which can react with $CO_2$ and TFE to catalyze the conversion of $CO_2$ to CO and $H_2O$, where one equivalent of $H^+$ is derived from the macrocyclic framework. Other reductive deprotonation processes such HER are also feasible and similarly result in a singly deprotonated active catalyst.

## CONCLUSIONS

We have isolated and characterized two deprotonated derivatives of the $CO_2$ reduction catalyst **Co(L)**, one with two deprotonated amines, **Co($L^{2-}$)**, and one with four deprotonated amines, **Co($L^{4-}$)**. Examination of the crystal structure reveals delocalization of the resultant negative charge into the ligand framework resulting in changes to the cobalt coordination environment and more subtlety solution state structure formation of intermolecular clusters. Titration experiments with the weak acid TFE reveals the first $pK_a$ of **Co(L)** is 20.55 ± 0.06 in DMF, or 20.50 ± 0.06 in DMSO, indicating the active catalyst is singly deprotonated under previously reported catalytic conditions (1.5 M TFE, 0.5 mM [Co]). Cyclic voltammetry show **Co($L^{4-}$)** is able to yield a catalytic current response in the presence of $CO_2$ and TFE while maintaining high selectivity for $CO_2$ to CO conversion. These results reveal the physical underpinnings of the linear correlation between $n_{donor} - 1$ and catalytic activity and highlight the subtle interplay and mechanistic consequences when paring exogenous acids with pendant proton relays.

## EXPERIMENTAL

**General Considerations.** All manipulation of air and moisture sensitive materials were conducted under a nitrogen atmosphere in a Vacuum Atmospheres drybox or on a dual manifold Schlenk line. All glassware was oven-dried prior to use. All solvents were degassed with nitrogen and passed through activated alumina columns and stored over 4Å Linde-type molecular sieves. Deuterated solvents were dried over 4Å Linde-type molecular sieves prior to use with the exception of DMF-$d_7$, which was received in flame-sealed ampoules and used as received. All NMR spectra were acquired at room temperature using Varian (Mercury 400 2-Channel, VNMRS-500 2-Channel, VNMRS- 600 3-Channel, and 400-MR 2-Channel) spectrometers. Proton NMR spectra are referenced to the residual $^1$H resonances of the deuterated solvent and are reported as parts per million relative to tetramethylsilane. Paramagnetic proton NMR spectra are referenced to the residual $^1$H resonances of the pure deuterated solvent in a flame sealed capillary inserted into the analyte solution. Cyclic voltammetry and controlled potential electrolysis experiments were performed using a Pine WaveDriver 20 potentiostat. UV-vis experiments were performed on a PerkinElmer Lambda 950 UV-vis-NIR spectrophotometer. FTIR experiments were performed on a Bruker Vertex 80V FT-IR spectrometer. SEM/EDS experiments were performed using a Thermo-Scientific Helios G4 PFIB UXe electron microscope equipped with an Oxford UltimMax 170 Silicon Drift Detector x-ray energy dispersive spectroscopy system. Elemental analyses were performed by Robertson Microlit Laboratories Ledgewood, New Jersey. All the chemical reagents were purchased from commercial vendors and used without further purification unless otherwise noted. Electrolyte (tetrabutylammonium hexafluorophosphate) was recrystallized prior to use for electrochemical experiments. **Co(L)** was synthesized according to previously reported literature procedures.[45]

**$Na_2$[$Co^{II}$($L^{4-}$)] (Co($L^{4-}$)).** In an $N_2$ filled drybox [Co(L)(acetone)$_2$]($BF_4$)$_2$ (38.1 mg, 0.053 mmol) was added to a scintillation vial and combined with solid NaH (60% wt. in paraffin) (42.4 mg, 1.06 mmol, 20.0 equiv.) and a magnetic stirbar. DMF (2 mL) was added and the suspension was stirred over 3 days changing from a deep amber color to dark purple-brown. The suspension was then passed through a microfiber filter. X-ray diffraction quality crystals were obtained through vapor diffusion of $Et_2O$ into the reaction mixture, yielding the title compound as dark purple-brown needles (27.3 mg, 0.034 mmol, 64.5% yield). $^1$H NMR, 500 MHz (DMSO-$d_6$): δ 9.74 (s, 4H), −1.81 (br s, 8H). Anal calcd for [$Na_2$[Co($L^{4-}$)]•3DMF•$H_2O$ ½ $Et_2O$ ½ $NaBF_4$ ($C_{31}H_{40}B_{0.5}F_2N_{11}Na_{2.5}O_{4.5}$): C, 46.63; H, 5.05; N, 19.29. Found: C, 46.29; H, 4.85; N, 18.73.

**[Co($L^{2-}$)($C_6D_5N$)$_2$] (Co($L^{2-}$)).** In an $N_2$ filled drybox [Co(L)(acetone)$_2$]($BF_4$)$_2$ (6.3 mg, 0.0088 mmol) was dissolved in in pyridine-$d_5$. To this solution excess NaH (60% wt. in paraffin) was added (1.0 mg, 0.025 mmol, 2.8 equiv.) and the suspension was transferred to a J-Young NMR tube and sealed. The J-Young tube was brought out of the drybox, sonicated for approximately 1 hour, and monitored by $^1$H NMR spectroscopy to ensure all the features corresponding to the starting material had disappeared. After the reaction had gone to completion, the J-Young tube was transferred back to the drybox, and the suspension was filtered. Overnight diffusion of diethyl ether into the reaction mixture produced a dark red crystalline solid (2.1 mg, 0.0032 mmol, 36% yield). $^1$H NMR (400 MHz, DMSO-$d_6$): δ 9.56 (s, 4H), −1.23 (br, s, 8H). Anal. calcd for [Co($L^{2-}$)($C_6D_5N$)$_2$]·($Et_2O$) ($C_{34}H_{33}CoN_{10}O$): C, 62.10 H, 5.21; N, 21.30. Found: C, 61.90; H, 4.16; N, 20.76.

**$^1$H NMR Titration of $Na_2$[$Co^{II}$($L^{4-}$)] with HOTf•DMF.** In an $N_2$ filled drybox **$Na_2$[$Co^{II}$($L^{4-}$)]** (2.9 mg, 0.0036 mmol) was dissolved in 0.7 mL DMSO-$d_6$ (5.2 mM). The dark amber solution was transferred to a J-Young tube, brought out of the drybox, and a $^1$H NMR spectrum was collected. The sample was then transferred back to the drybox, where HOTf•DMF (27 mL, 1.02 equiv.) was titrated in from a stock solution of HOTf•DMF in DMSO-$d_6$ (15.2 mg in 0.5 mL, 136.2 mM). The J-Young tube was then sealed, mixed via inversion and brought out, and another $^1$H NMR spectrum was collected. The above titration procedure was then repeated, for 2, 3, 4, and 6 equivalents of HOTf•DMF added.

**Variable Temperature $^1$H NMR Spectroscopy.** In an $N_2$ filled drybox **$Na_2$[$Co^{II}$($L^{4-}$)]** (6.0 mg, 0.0076 mmol) was dissolved in 0.7 mL DMF-$d_7$ (10.8 mM). The dark amber solution was transferred to a J-Young tube and a capillary containing pure DMF-$d_7$ was inserted. The sample brought out of the drybox, and placed into the $^1$H NMR spectrometer cooled to 218 K. The temperature was allowed to equilibrate for 10 minutes prior to data collection. This process was repeated at 233 K, 248 K, 263 K, 273 K and 298 K.

**Spectrophotometric Titration of $Na_2$[$Co^{II}$($L^{4-}$)] with HOTf•DMF.** In an $N_2$ filled drybox a stock solution of **$Na_2$[$Co^{II}$($L^{4-}$)]** was prepared by dissolving 1.4 mg (0.0018 mmol) of the metal complex in 10 mL DMF ([Co] = 0.18 mM). 2 mL of this stock solution was taken and diluted to 10 mL ([Co] = 35 mM). 2.5 mL of the diluted stock was transfer to a cuvette fitted with a PTFE valve and sealed under $N_2$. The cuvette was transferred out of the drybox and to a UV-vis spectrophotometer, where an absorption spectrum was collected. The cuvette was then brought back into the drybox where HOTf•DMF in DMF (8.2 mM) was added (10 mL, 0.9 equiv.), and the absorption spectrum subsequently re-measured. This process was repeated, titrating in 1.9, 2.8, 3.8, 5.6 and 940 equivalents of HOTf•DMF.

**Spectrophotometric Determination $[Co^{II}(L)]^{2+}$ p$K_a$[1].** In an $N_2$ filled drybox **$Na_2[Co^{II}(L^{4-})]$** (1.1 mg, 0.0014 mmol) was dissolved in 10 mL of DMF ([Co] = 0.14 mM). To a cuvette fitted with a PTFE valve, 0.8 mL of the stock solution was added and diluted to 2.5 mL with DMF ([Co] = 44 μM) and sealed. The cuvette was taken out of the box, and its absorbance features were measured on a UV-vis spectrophotometer. The cuvette was then brought back into the glovebox, and 2,2,2-trifluoroethanol (TFE) was titrated in ([TFE] = 0.01, 0.10, 0.31, 0.65 and 1.29 M) and measuring the absorbance features after every aliquot of TFE. A p$K_a$ value was determined from measuring the absorbance at 334 nm at 0.31 M TFE to establish the speciation of **$[Co(L)]^{2+}$** ($\varepsilon_{344}$ = 44,800 $M^{-1}$ $cm^{-1}$, see **Figure S23**) from which **$[Co(L^{-})]^{+}$**, **[TFE]** and **$[TFE]^{-}$**, are extrapolated and $K_a$ and p$K_a$ are calculated. The p$K_a$ was calculated under the assumption that all the cobalt complex exists in an equilibrium between the mono-deprotonated and fully protonated states, an assumption consistent when comparing the UV-vis spectra of **$Na_2[Co^{II}(L^{4-})]$** with 0.31 M TFE added, with that of **$Na_2[Co^{II}(L^{4-})]$** with addition of ~3 equivalents of strong acid HOTf•DMF. The above procedure was repeated in DMSO solvent using 3 mL of 36 μM **$Co(L^{4-})$** in 0.82 M TFE generating a binary system of **$[Co(L^{-})]^{+}$** and **$[Co(L)]^{2+}$.**

**Cyclic Voltammetry (CV).** Electrochemistry experiments were carried out using a Pine potentiostat running the Aftermath software (version 1.5.9885). The experiments were performed in a single compartment electrochemical cell under nitrogen or $CO_2$ atmosphere using a 3 mm diameter glassy carbon electrode as the working electrode, a platinum wire as auxiliary electrode and a silver wire as the reference electrode. Ohmic drop was measured via current interrupt experiments prior to each CV scan and input into aftermath for charge compensation. All reported potentials are referenced relative to ferrocene (Fc) with the $Fe^{3+/2+}$ couple at 0.0 V. All electrochemical experiments were performed with 0.1 M tetrabutylammonium hexafluorophosphate as supporting electrolyte. The concentrations of all cobalt complexes were generally at 0.5 mM and experiments with $CO_2$ were performed at gas saturation or varying amounts of $CO_2$ in dimethylformamide (DMF).

**Controlled Potential Electrolysis.** Controlled potential electrolysis (CPE) measurements were conducted in a two-chambered H cell under either 1 atmosphere of nitrogen or carbon dioxide. The first chamber, equipped with a PTFE stir bar, held the working and reference electrodes in 25 mL of 0.1 M tetrabutylammonium hexafluorophosphate and 1.5 M of 2,2,2,-trifluoroethanol in DMF. The second chamber held the auxiliary electrode in 40 mL of 0.1 M tetrabutylammonium hexafluorophosphate in DMF. The two chambers were separated by a fine porosity glass frit. The reference electrode (Ag wire in 0.1 M tetrabutylammonium hexafluorophosphate) was placed in a separate compartment and connected by a Vycor tip. Glassy carbon plate electrodes (6 cm × 1 cm × 0.3 cm; Tokai Carbon USA) were used as the working and auxiliary electrodes. CO and $H_2$ products were measured by withdrawing 2 mL of gas from the headspace of the H cell via gas tight syringe and injected into a gas chromatography instrument (Shimadzu GC-2010-Plus) equipped with a BID detector and a Restek Shin-Carbon ST Micropacked column. Faradaic efficiencies were determined by diving the measured moles of CO or $H_2$ detected (based off a calibration curve of known authentic standards) and divided by the moles of electrons passed during the controlled potential electrolysis experiment. For each species the controlled-potential electrolysis measurements were performed at least twice, leading to similar behavior.

**Evans Method Experiments**. Evans method measurements were accomplished by dissolving the cobalt complex in 0.7 mL of deuterated solvent (DMSO-$d_6$ or DMF-$d_7$) in an inert atmosphere glovebox. The solution was transferred to an NMR or J-Young tube and a sealed capillary containing pure deuterated solvent was inserted into the cobalt solution (if an ordinary NMR tube was used, the cap was subsequently sealed with parafilm). A $^1$H NMR spectrum was then collected on a 500 MHz spectrometer. The corrected molar susceptibility ($X_P$) was calculated based on the shift of the residual solvent resonances in the solution of the complex *vs.* that found in the internal capillary using the equation below where $\Delta f$ is the observed $^1$H NMR shift of the reference standard in Hz, C is the concentration of the sample in mol/L, $f$ is the proton Larmor frequency (500,000,000 Hz), and $X_D$ is the diamagnetic susceptibility correction factor (calc. $-4.32 \times 10^{-5}$ $\mu_B$).

$$X_P = \frac{3000 \times \Delta f}{4\pi C f} - X_D$$

The effective magnetic moment was calculated using the equation below where T is the temperature in Kelvin, $X_P$ is the corrected molar susceptibility, and $\mu_{eff}$ is the effective magnetic moment in Bohr Magnetons.

$$\mu_{eff} = 2.84\sqrt{T \times X_P}$$

**X-ray Diffraction Data Collection and Processing.** The X-ray intensity data were collected on a Bruker APEX DUO 3-circle platform diffractometer with the χ-axis fixed at 50.74°, and using Mo $K_\alpha$ radiation (λ = 0.71073 Å) from a fine-focus tube monochromatized by a TRIUMPH curved-crystal monochromator.[58] The diffractometer was equipped with an APEX II CCD detector and an Oxford Cryosystems Cryostream 700 apparatus for low-temperature data collection adjusted to 173(2) K. The crystal was mounted in a Cryo-Loop using Paratone oil. A complete hemisphere of data was scanned on omega (0.5°) at a detector distance of 50 mm and a resolution of 512 × 512 pixels. The frames were integrated using the SAINT algorithm[59] to give the hkl files corrected for Lp/decay. Data were corrected for absorption effects using the multi-scan method (SADABS).[60] The structures were solved by intrinsic phasing and refined with the Bruker SHELXTL Software Package.[61–64] The structure of $Co(L^{2-})$ was refined in the hexagonal space group $P6_522$ as a 2-component inversion twin with a refined twin ratio of 92:8. The crystal contained embedded pyridine molecules that were disordered and did not refine well. The contributions of these molecules were mapped using the Squeeze algorithm.[65] A total of 399 electrons were mapped in the cell which corresponds to approximately 1.5 pyridine molecules per **$Co(L^{2-})$** molecule.

## ASSOCIATED CONTENT

### Supporting Information

The Supporting Information is available free of charge on the ACS Publications website.

Supplemental information including additional electrochemical experiments, $pK_a$ calculations, variable temperature NMR spectra and X-ray structure refinement. (PDF)
Crystallographic data for **$Co(L^{2-})$** (CIF)
Crystallographic data for **$Co(L^{4-})$** (CIF)

## AUTHOR INFORMATION

**Corresponding Author**
* E-mail: smarines@usc.edu

**ORCID**
Jeffrey J. Liu: 0000-0003-2147-6449
Alon Chapovetsky: 0000-0001-8095-8830
Ralf Haiges: 0000-0003-4151-3593
Smaranda C. Marinescu: 0000-0003-2106-8971

**Author Contributions**
The manuscript was written through contributions of all authors.

**Notes**
The authors declare no competing financial interest.

## ACKNOWLEDGMENT

The research was primarily supported by the National Science Foundation (NSF) under the CAREER Award CHE-1555387 and CHE-2102707. SCM acknowledges additional support from the Alfred P. Sloan Foundation through a Sloan research fellowship, the University of Southern California (USC), and the USC Women in Science and Engineering program. JJL would like to thank the USC Wrigely Institute for Environmental Studies for the Hagenah postdoctoral fellowship in support of this work.

## REFERENCES

(1) Jackson, R. B.; Le Quéré, C.; Andrew, R. M.; Canadell, J. G.; Korsbakken, J. I.; Liu, Z.; Peters, G. P.; Zheng, B. Global Energy Growth Is Outpacing Decarbonization. *Environ. Res. Lett.* **2018**, *13*, 120401.

(2) Senftle, T. P.; Carter, E. A. The Holy Grail: Chemistry Enabling an Economically Viable $CO_2$ Capture, Utilization, and Storage Strategy. *Acc. Chem. Res.* **2017**, *50*, 472–475.

(3) Benson, E. E.; Kubiak, C. P.; Sathrum, A. J.; Smieja, J. M. Electrocatalytic and Homogeneous Approaches to Conversion of $CO_2$ to Liquid Fuels. *Chem. Soc. Rev.* **2009**, *38*, 89–99.

(4) Francke, R.; Schille, B.; Roemelt, M. Homogeneously Catalyzed Electroreduction of Carbon Dioxide - Methods, Mechanisms, and Catalysts. *Chem. Rev.* **2018**, *118*, 4631–4701.

(5) Barlow, J. M.; Yang, J. Y. Thermodynamic Considerations for Optimizing Selective $CO_2$ Reduction by Molecular Catalysts. *ACS Cent. Sci.* **2019**, *5*, 580–588.

(6) Fujita, E.; Creutz, C.; Sutin, N.; Szalda, D. J. Carbon Dioxide Activation by Cobalt(I) Macrocycles: Factors Affecting Carbon Dioxide and Carbon Monoxide Binding. *J. Am. Chem. Soc.* **1991**, *113*, 343–353.

(7) Schmeier, T. J.; Dobereiner, G. E.; Crabtree, R. H.; Hazari, N. Secondary Coordination Sphere Interactions Facilitate the Insertion Step in an Iridium(III) $CO_2$ Reduction Catalyst. *J. Am. Chem. Soc.* **2011**, *133*, 9274–9277.

(8) Azcarate, I.; Costentin, C.; Robert, M.; Savéant, J. M. Through-Space Charge Interaction Substituent Effects in Molecular Catalysis Leading to the Design of the Most Efficient Catalyst of $CO_2$-to-CO Electrochemical Conversion. *J. Am. Chem. Soc.* **2016**, *138*, 16639–16644.

(9) Ngo, K. T.; McKinnon, M.; Mahanti, B.; Narayanan, R.; Grills, D. C.; Ertem, M. Z.; Rochford, J. Turning on the Protonation-First Pathway for Electrocatalytic $CO_2$ Reduction by Manganese Bipyridyl Tricarbonyl Complexes. *J. Am. Chem. Soc.* **2017**, *139*, 2604–2618.

(10) Clark, M. L.; Cheung, P. L.; Lessio, M.; Carter, E. A.; Kubiak, C. P. Kinetic and Mechanistic Effects of Bipyridine (Bpy) Substituent, Labile Ligand, and Brønsted Acid on Electrocatalytic $CO_2$ Reduction by Re(Bpy) Complexes. *ACS Catal.* **2018**, *8*, 2021–2029.

(11) Ahmed, M. E.; Rana, A.; Saha, R.; Dey, S.; Dey, A. Homogeneous Electrochemical Reduction of $CO_2$ to CO by a Cobalt Pyridine Thiolate Complex. *Inorg. Chem.* **2020**.

(12) Hull, J. F.; Himeda, Y.; Wang, W. H.; Hashiguchi, B.; Periana, R.; Szalda, D. J.; Muckerman, J. T.; Fujita, E. Reversible Hydrogen Storage Using $CO_2$ and a Proton-Switchable Iridium Catalyst in Aqueous Media under Mild Temperatures and Pressures. *Nat. Chem.* **2012**, *4*, 383–388.

(13) Chabolla, S. A.; Dellamary, E. A.; Machan, C. W.; Tezcan, F. A.; Kubiak, C. P. Combined Steric and Electronic Effects of Positional Substitution on Dimethyl-Bipyridine Rhenium(I)Tricarbonyl Electrocatalysts for the Reduction of $CO_2$. *Inorganica Chim. Acta* **2014**, *422*, 109–113.

(14) Sampson, M. D.; Nguyen, A. D.; Grice, K. A.; Moore, C. E.; Rheingold, A. L.; Kubiak, C. P. Manganese Catalysts with Bulky Bipyridine Ligands for the Electrocatalytic Reduction of Carbon Dioxide: Eliminating Dimerization and Altering Catalysis. *J. Am. Chem. Soc.* **2014**, *136*, 5460–5471.

(15) Nichols, E. M.; Chang, C. J. Urea-Based Multipoint Hydrogen-Bond Donor Additive Promotes Electrochemical $CO_2$ Reduction Catalyzed by Nickel Cyclam. *Organometallics* **2019**, *38*, 1213–1218.

(16) Parkin, A.; Seravalli, J.; Vincent, K. A.; Ragsdale, S. W.; Armstrong, F. A. Rapid and Efficient Electrocatalytic $CO_2$ /CO Interconversions by Carboxydothermus Hydrogenoformans CO Dehydrogenase I on an Electrode. *J. Am. Chem. Soc.* **2007**, *129*, 10328–10329.

(17) Jeoung, J.-H.; Dobbek, H. Carbon Dioxide Activation at the Ni,Fe-Cluster of Anaerobic Carbon Monoxide Dehydrogenase. *Science* **2007**, *318*, 1461–1464.

(18) Domnik, L.; Merrouch, M.; Goetzl, S.; Jeoung, J. H.; Léger, C.; Dementin, S.; Fourmond, V.; Dobbek, H. CODH-IV: A High-Efficiency CO-Scavenging CO Dehydrogenase with Resistance to $O_2$. *Angew. Chemie - Int. Ed.* **2017**, *56*, 15466–15469.

(19) Gordon, Z.; Miller, T. J.; Leahy, C. A.; Matson, E. M.; Burgess, M.; Drummond, M. J.; Popescu, C. V.; Smith, C. M.; Lord, R. L.; Rodríguez-López, J.; et al. Characterization of Terminal Iron(III)-Oxo and Iron(III)-Hydroxo Complexes Derived from O2 Activation. *Inorg. Chem.* **2019**, *58*, 15801–15811.

(20) Shanahan, J. P.; Szymczak, N. K. Hydrogen Bonding to a Dinitrogen Complex at Room Temperature: Impacts on $N_2$ Activation. *J. Am. Chem. Soc.* **2019**, *141*, 8550–8556.

(21) Roy, S. S.; Talukdar, K.; Jurss, J. W. Electro- and Photochemical Reduction of $CO_2$ by Molecular Manganese Catalysts: Exploring the Positional Effect of Second-Sphere Hydrogen-Bond Donors. *ChemSusChem* **2021**, *14*, 662–670.

(22) Cook, S. A.; Borovik, A. S. Molecular Designs for Controlling the Local Environments around Metal Ions. *Acc. Chem. Res.* **2015**, *48*, 2407–2414.

(23) Costentin, C.; Drouet, S.; Robert, M.; Savéant, J.-M. A Local Proton Source Enhances $CO_2$ Electroreduction to CO by a Molecular Fe Catalyst. *Science* **2012**, *338*, 90–94.

(24) Adam, S. M.; Wijeratne, G. B.; Rogler, P. J.; Diaz, D. E.; Quist, D. A.; Liu, J. J.; Karlin, K. D. Synthetic Fe/Cu Complexes: Toward Understanding Heme-Copper Oxidase Structure and Function. *Chem. Rev.* **2018**, *118*, 10840–11022.

(25) Dahl, E. W.; Dong, H. T.; Szymczak, N. K. Phenylamino Derivatives of Tris(2-Pyridylmethyl)Amine: Hydrogen-Bonded

Peroxodicopper Complexes. *Chem. Commun.* **2018**, *54*, 892–895.

(26) Diaz, D. E.; Quist, D. A.; Herzog, A. E.; Schaefer, A. W.; Kipouros, I.; Bhadra, M.; Solomon, E. I.; Karlin, K. D. Impact of Intramolecular Hydrogen Bonding on the Reactivity of Cupric Superoxide Complexes with O−H and C−H Substrates. *Angew. Chemie Int. Ed.* **2019**, *58*, 17572–17576.

(27) Oswald, V. F.; Lee, J. L.; Biswas, S.; Weitz, A. C.; Mittra, K.; Fan, R.; Li, J.; Zhao, J.; Hu, M. Y.; Alp, E. E.; et al. Effects of Noncovalent Interactions on High-Spin Fe(IV)-Oxido Complexes. *J. Am. Chem. Soc.* **2020**, *142*, 11804–11817.

(28) Agarwal, J.; Shaw, T. W.; Schaefer, H. F.; Bocarsly, A. B. Design of a Catalytic Active Site for Electrochemical $CO_2$ Reduction with Mn(I)-Tricarbonyl Species. *Inorg. Chem.* **2015**, *54*, 5285–5294.

(29) Sung, S.; Kumar, D.; Gil-Sepulcre, M.; Nippe, M. Electrocatalytic $CO_2$ Reduction by Imidazolium-Functionalized Molecular Catalysts. *J. Am. Chem. Soc.* **2017**, *139*, 13993–13996.

(30) Hellman, A. N.; Haiges, R.; Marinescu, S. C. Rhenium Bipyridine Catalysts with Hydrogen Bonding Pendant Amines for $CO_2$ Reduction. *Dalt. Trans.* **2019**, *48*, 14251–14255.

(31) Zee, D. Z.; Nippe, M.; King, A. E.; Chang, C. J.; Long, J. R. Tuning Second Coordination Sphere Interactions in Polypyridyl–Iron Complexes to Achieve Selective Electrocatalytic Reduction of Carbon Dioxide to Carbon Monoxide. *Inorg. Chem.* **2020**, *59*, 5206–5217.

(32) Nichols, A. W.; Machan, C. W. Secondary-Sphere Effects in Molecular Electrocatalytic $CO_2$ Reduction. *Front. Chem.* **2019**, *7*, 1–19.

(33) Nichols, E. M.; Derrick, J. S.; Nistanaki, S. K.; Smith, P. T.; Chang, C. J. Positional Effects of Second-Sphere Amide Pendants on Electrochemical $CO_2$ Reduction Catalyzed by Iron Porphyrins. *Chem. Sci.* **2018**, *9*, 2952–2960.

(34) Talukdar, K.; Sinha Roy, S.; Amatya, E.; Sleeper, E. A.; Le Magueres, P.; Jurss, J. W. Enhanced Electrochemical $CO_2$ Reduction by a Series of Molecular Rhenium Catalysts Decorated with Second-Sphere Hydrogen-Bond Donors. *Inorg. Chem.* **2020**, acs.inorgchem.0c00154.

(35) Taylor, J. O.; Neri, G.; Banerji, L.; Cowan, A. J.; Hartl, F. Strong Impact of Intramolecular Hydrogen Bonding on the Cathodic Path of [Re(3,3′-Dihydroxy-2,2′-Bipyridine)$(CO)_3$Cl] and Catalytic Reduction of Carbon Dioxide. *Inorg. Chem.* **2020**.

(36) Beley, M.; Collin, J.-P.; Ruppert, R.; Sauvage, J.-P. Nickel(II)-Cyclam: An Extremely Selective Electrocatalyst for Reduction of $CO_2$ in Water. *J. Chem. Soc. Chem. Commun.* **1984**, *2*, 1315.

(37) Froehlich, J. D.; Kubiak, C. P. Homogeneous $CO_2$ Reduction by Ni(Cyclam) at a Glassy Carbon Electrode. *Inorg. Chem.* **2012**, *51*, 3932–3934.

(38) Haviv, E.; Azaiza-Dabbah, D.; Carmieli, R.; Avram, L.; Martin, J. M. L.; Neumann, R. A Thiourea Tether in the Second Coordination Sphere as a Binding Site for $CO_2$ and a Proton Donor Promotes the Electrochemical Reduction of $CO_2$ to CO Catalyzed by a Rhenium Bipyridine-Type Complex. *J. Am. Chem. Soc.* **2018**, *140*, 12451–12456.

(39) Roy, S.; Sharma, B.; Pécaut, J.; Simon, P.; Fontecave, M.; Tran, P. D.; Derat, E.; Artero, V. Molecular Cobalt Complexes with Pendant Amines for Selective Electrocatalytic Reduction of Carbon Dioxide to Formic Acid. *J. Am. Chem. Soc.* **2017**, *139*, 3685–3696.

(40) Sung, S.; Li, X.; Wolf, L. M.; Meeder, J. R.; Bhuvanesh, N. S.; Grice, K. A.; Panetier, J. A.; Nippe, M. Synergistic Effects of Imidazolium-Functionalization on Fac-Mn$(CO)_3$ Bipyridine Catalyst Platforms for Electrocatalytic Carbon Dioxide Reduction. *J. Am. Chem. Soc.* **2019**, *141*, 6569–6582.

(41) Nichols, A. W.; Hooe, S. L.; Kuehner, J. S.; Dickie, D. A.; Machan, C. W. Electrocatalytic $CO_2$ Reduction to Formate with Molecular Fe(III) Complexes Containing Pendent Proton Relays. *Inorg. Chem.* **2020**, *59*, 5854–5864.

(42) Loewen, N. D.; Berben, L. A. Secondary Coordination Sphere Design to Modify Transport of Protons and $CO_2$. *Inorg. Chem.* **2019**, *58*, 16849–16857.

(43) Savéant, J. M. Proton Relays in Molecular Catalysis of Electrochemical Reactions: Origin and Limitations of the Boosting Effect. *Angew. Chemie - Int. Ed.* **2019**, *58*, 2125–2128.

(44) Hellman, A. N.; Haiges, R.; Marinescu, S. C. Rhenium Bipyridine Catalysts with Hydrogen Bonding Pendant Amines for $CO_2$ Reduction. *Dalt. Trans.* **2019**, *48*, 14251–14255.

(45) Chapovetsky, A.; Do, T. H.; Haiges, R.; Takase, M. K.; Marinescu, S. C. Proton-Assisted Reduction of $CO_2$ by Cobalt Aminopyridine Macrocycles. *J. Am. Chem. Soc.* **2016**, *138*, 5765–5768.

(46) Chapovetsky, A.; Welborn, M.; Luna, J. M.; Haiges, R.; Miller, T. F.; Marinescu, S. C. Pendant Hydrogen-Bond Donors in Cobalt Catalysts Independently Enhance $CO_2$ Reduction. *ACS Cent. Sci.* **2018**, *4*, 397–404.

(47) Chapovetsky, A.; Liu, J. J.; Welborn, M.; Luna, J. M.; Do, T.; Haiges, R.; Miller, T. F.; Marinescu, S. C.; Miller III, T. F.; Marinescu, S. C. Electronically Modified Cobalt Aminopyridine Complexes Reveal an Orthogonal Axis for Catalytic Optimization for $CO_2$ Reduction. *Inorg. Chem.* **2020**, *59*, 13709–13718.

(48) Goodwin, H. A. Spin Crossover in Cobalt(II) Systems. In *Spin Crossover in Transition Metal Compounds II*; 2012; pp 23–47.

(49) Herschlag, D.; Pinney, M. Hydrogen Bonds: Simple after All? *Biochemistry* **2018**, *57*, 3338–3352.

(50) Addison, A. W.; Rao, T. N.; Reedijk, J.; van Rijn, J.; Verschoor, G. C. Synthesis, Structure, and Spectroscopic Properties. *J. Chem. Soc. Dalt. Trans.* **1984**, *251*, 1349–1356.

(51) Yang, L.; Powell, D. R.; Houser, R. P. Structural Variation in Copper(I) Complexes with Pyridylmethylamide Ligands: Structural Analysis with a New Four-Coordinate Geometry Index, T4. *Dalt. Trans.* **2007**, No. 9, 955–964.

(52) Cotton, F. A.; Wilkinson, G. *Advanced Inorganic Chemistry*, 4th ed.; Wiley: New York, 1980.

(53) Bordwell, F. G. Equilibrium Acidities in Dimethyl Sulfoxide Solution. *Acc. Chem. Res.* **1988**, *21*, 456–463.

(54) Lam, Y. C.; Nielsen, R. J.; Gray, H. B.; Goddard, W. A. A Mn Bipyrimidine Catalyst Predicted to Reduce $CO_2$ at Lower Overpotential. *ACS Catal.* **2015**, *5*, 2521–2528.

(55) Lee, K. J.; McCarthy, B. D.; Dempsey, J. L. On Decomposition, Degradation, and Voltammetric Deviation: The Electrochemist's Field Guide to Identifying Precatalyst Transformation. *Chem. Soc. Rev.* **2019**, *48*, 2927–2945.

(56) Pegis, M. L.; Roberts, J. A. S.; Wasylenko, D. J.; Mader, E. A.; Appel, A. M.; Mayer, J. M. Standard Reduction Potentials for Oxygen and Carbon Dioxide Couples in Acetonitrile and N,N-Dimethylformamide. *Inorg. Chem.* **2015**, *54*, 11883–11888.

(57) Queyriaux, N.; Sun, D.; Fize, J.; Pécaut, J.; Field, M. J.; Chavarot-Kerlidou, M.; Artero, V. Electrocatalytic Hydrogen Evolution with a Cobalt Complex Bearing Pendant Proton Relays: Acid Strength and Applied Potential Govern Mechanism and Stability. *J. Am. Chem. Soc.* **2020**, *142*, 274–282.

(58) Bruker Instrument Service V2011.4.0.0, Bruker AXS, Madison, WI. 2011.

(59) SAINT+ V8.27B, Bruker AXS Madison, WI. 2011.

(60) SADABS V2012-1, Bruker AXS Madison, WI, 2012.

(61) Bruker SHELXTL V2014/7, Bruker AXS Madison, WI. 2014.

(62) Sheldrick, G. M. A Short History of SHELX. *Acta Crystallogr. Sect. A Found. Crystallogr.* **2008**, *64*, 112–122.

(63) Sheldrick, G. M. Crystal Structure Refinement with SHELXL. *Acta Crystallogr. Sect. C Struct. Chem.* **2015**, *71*, 3–8.

(64) Hübschle, C. B.; Sheldrick, G. M.; Dittrich, B. ShelXle: A Qt Graphical User Interface for SHELXL. *J. Appl. Crystallogr.* **2011**, *44*, 1281–1284.

(65) Spek, A. L. PLATON SQUEEZE: A Tool for the Calculation of the Disordered Solvent Contribution to the Calculated Structure Factors. *Acta Crystallogr. Sect. C Struct. Chem.* **2015**, *71*, 9–18.

TOC Graphic:

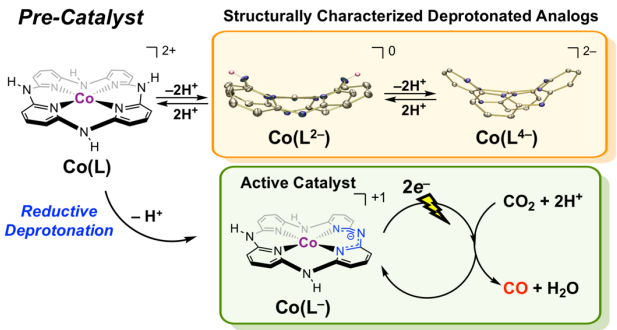


<u>Synopsis:</u>

Incorporation of H-bond donors into catalyst ligand frameworks has been demonstrated as an effective strategy for optimizing the $CO_2$ reduction reaction. However, not as frequently discussed is whether these donors exhibit prolonged acid/base stability over the course of catalysis, and what effects deprotonation may have on catalysis. We report here the isolation, and characterization of two deprotonated derivatives of **Co(L)**, an electrocatalyst for $CO_2$-to-CO conversion, and investigate dynamics of catalysis on H-bond donor protonation state.